11th International Symposium on Turbulence and Shear Flow Phenomena (TSFP11)
Southampton, UK, July 30 to August 2, 2019

END EFFECTS OF NOMINALLY TWO DIMENSIONAL THIN FLAT PLATES

Kaden Agrey, Eric Braun, Robert J. Martinuzzi
Department of Mechanical and Manufacturing Eng.
University of Calgary
2500 University Dr. NW, Calgary, Alberta, Canada
kbagrey@ucalgary.ca, eabraun@ucalgary.ca, rmartinu@ucalgary.ca

ABSTRACT

Differences in the structure and dynamics of nominally two-dimensional turbulent wakes are investigated experimentally for a thin flat plate, normal to a uniform flow, with two different end conditions: with and without endplates. Both cases are characterized by Karman-like vortex shedding and have a two-dimensional mean flow field. A low frequency flapping mode is observed in addition to the base flow drift motion typical of cylinder wakes. For the case without endplates, an interaction between the drift motion and the vortex formation process is associated with a much stronger modulation of the quasi-periodic vortex shedding amplitude when compared to the case with endplates. These dynamics underlie structural differences in the mean wake and Reynolds stress fields.

INTRODUCTION

Experimental studies have shown that achieving mean two-dimensional wakes is challenging and subject to subtle effects, even for high aspect ratio bodies. For the case of bluff bodies, Williamson (1989) demonstrated that three dimensionality can be reduced by adding endplates, thereby imposing a closed end condition (CE). This addition to the geometry was found to have strong effects near the ends and to influence the remaining flow-field indirectly. Williamson described how single vortices shed off of bluff bodies with open ends (that is, without endplates) can feature many cells with distinct frequencies. When these vortex cells are out of phase, vortex dislocations appear and vortices are shed obliquely. These oblique vortices change the Strouhal number (Williamson (1989)) and are accompanied by a small mean spanwise velocity component (Hammache & Gharib (1991)). Hammache & Gharib (1991) noted that when parallel vortex shedding occurs, the base pressure along the span of the body is symmetric. Closed ends can eliminate these cells, force the necessary boundary conditions for parallel shedding, and eliminate the spanwise velocity. This change in dynamics can be partly attributed to the endplates' impact on the separation point on the cylinder surface. Despite these differences, the observed changes to the mean velocity and Reynolds stress fields were subtle.

The normal flat plate has received less attention than the cylinder. Experiments by Mohebi *et al.* (2017), using a flat plate with a high aspect ratio and open ends, show a nominally two-dimensional mean flow field, parallel vortex shedding, and a spanwise symmetric base pressure. Nevertheless, when compared with numerical investigations for an infinite normal flat plate (Hemmati *et al.* (2018, 2016); Najjar & Balachandar (1998)), the wake structure, Strouhal number (St), and coefficient of drag (C_D) are significantly different. For experiments with closed ends, the 2D mean field, St, and C_D are more similar to those from simulations. Regardless of end conditions, separation is fixed at the flat plate edges and shedding is parallel. Moreover, the influence of the Reynolds number (Re) on St and C_D is small for $Re > 1000$, Hemmati *et al.* (2018).

A low frequency unsteadiness in the wake can be observed (Fage & Johansen (1927)) or is discussed (Najjar & Balachandar (1998); Hemmati *et al.* (2016); Kiya & Matsumura (1988); Lisoski (1993)) in many reported flat plate flows. Low frequency modulations in the shedding process are identified in the examined flows. These modulations are expected to influence energy transfer between scales and thus the mean wake structure. In laminar, two-dimensional cylinder wakes, Noack *et al.* (2003) showed an exchange of energy between shed vortices and a slowly varying base flow, modeled by a Stuart-Landau mean field oscillator. Bourgeois *et al.* (2013) showed that this relationship also holds in the turbulent regime. It is thus hypothesized that the mean wake and Reynolds stress field structural differences observed for the plate flows are linked to changes in the dynamics relating different scales of motion.

In this study, the effect of endplates on a flat plate are investigated. In particular, differences in the Reynolds stress field structure are related to the wake dynamics. A modal decomposition of the wake velocity fluctuations shows the existence of two low frequency modes of motion. Their relationship to the shedding process is examined.

METHODOLOGY

The near-wake flows behind high aspect ratio (span-to-chord, $s/c > 40$) thin flat plates normal to a uniform stream of velocity U_∞ are considered for two conditions: open ends (OE), without end plates; and closed ends (CE), with end plates isolating the recirculation region from the ambient pressure. Experiments were conducted in an open jet suction-type wind tunnel of free stream turbulence below 0.5%. The flow geometry and measurement domain are defined in Fig. 1. The Cartesian coordinates in the streamwise, flow-normal, and spanwise directions are denoted (x,y,z) with their corresponding velocity components (u,v,w), respectively.

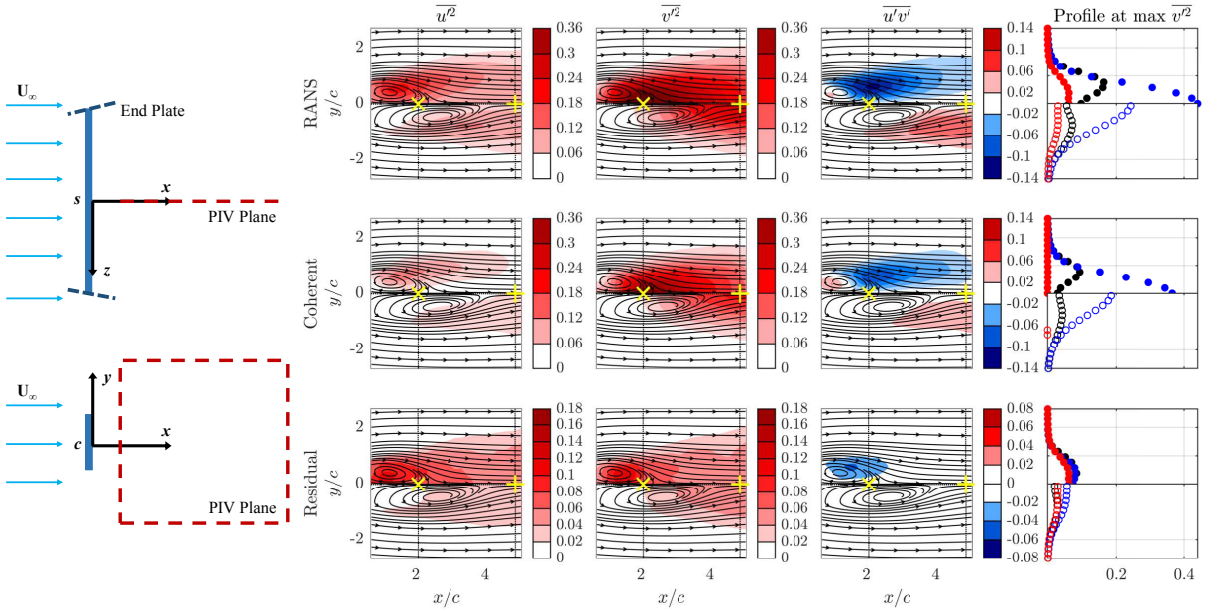

Figure 1. Definition sketch (left). Reynolds stress contours with overlaid mean streamlines (right). Top half-planes with closed ends, bottom half with open. A yellow **x** and **+** indicate points of maximum $\overline{v'^2}$ for cases with closed and open ends, respectively. The first row shows the RANS field; second is the coherent field; third is the residual field. Final column shows profiles at maximum $\overline{v'^2}$, open circles are for open ends, closed circles are closed ends. ▪ ▪ ▪ $\overline{u'^2}$, ▪ ▪ ▪ $\overline{v'^2}$, ▪ ▪ ▪ $\overline{w'^2}$.

The square rigid end plates consisted of 1.9 mm thick steel and were mounted normal to the test-plate at the edge of the working jet at $z = \pm 21c$ (Fig. 1). The plates extended to $x = -c$ upstream, $y = \pm 3c$ and $x = 5c$ downstream. The spanwise base pressure distribution was found to be sensitive to the end plate orientation. These were adjusted to an expanding angle of $\sim 2^\circ$ relative to the freestream, such that the mean base pressure and shedding phase were constant in the spanwise direction within experimental uncertainty.

Three component velocity fields were acquired using stereo particle image velocimitry (PIV). Planes at several spanwise locations were obtained to verify mean two-dimensional (2D) flow. The velocity fields were seeded using 1μm diameter olive oil particles and were sampled at a rate allowing at least 10 points per shedding cycle. Acquisition windows spanned approximately 600 shedding cycles. Experiments were performed in triplicate. PIV images were processed with DaVis Flow Master 8.3 software.

Experiments were conducted for $Re = U_\infty c/\nu$, with ν the kinematic viscosity of air, of 20000 (CE) and 6600 (OE). The shedding frequency, f_{sh}, corresponded to $St = f_{sh}c/U_\infty = 0.141$ (CE) and 0.119 (OE), while the mean base pressure $C_{Pb} = \overline{P_b - P_\infty}/\frac{1}{2}\rho U_\infty^2 = -1.3$ (CE) and -0.85 (OE), with ρ the density. In the following sections, velocity, Reynolds stress and vorticity are presented non-dimensionalized by U_∞, ρU_∞^2 and U_∞/c, respectively.

The velocity field was analyzed subject to a triple decomposition into mean, coherent and residual contributions:

$$\mathbf{u}(\mathbf{x},t) = \mathbf{U}(\mathbf{x}) + \underbrace{\mathbf{u}_c(\mathbf{x},t) + \mathbf{u}''(\mathbf{x},t)}_{\mathbf{u}'(\mathbf{x},\mathbf{t})} \qquad (1)$$

where $\mathbf{u}'$ represents the total fluctuations. Upright bold symbols indicate vectors and the argument $\mathbf{x}$ is position and t time. The coherent contribution is determined from a proper orthogonal decomposition (POD) of the flow field:

$$\mathbf{u}_c(\mathbf{x},t) = \sum_{n=1}^{N} a_n(t)\mathbf{\Phi}_n(\mathbf{x}) \qquad (2)$$

where a_n and $\mathbf{\Phi}_n$ are temporal and spatial modal functions. In subsequent sections, the arguments $\mathbf{x}$ and t are implied for compactness.

The spatial functions are orthonormal, satisfying:

$$(\mathbf{\Phi}_n, \mathbf{\Phi}_m) = \int_\Lambda (\mathbf{\Phi}_n \mathbf{\Phi}_m) \mathrm{d}x\mathrm{d}y = \delta_{nm}$$

where Λ is the PIV observation domain. The total kinetic energy of the fluctuations is thus given by:

$$\mathrm{TKE} = \frac{1}{2}\sum_n \lambda_n \quad , \quad \lambda_n = \overline{a_n^2}\,,$$

where λ_n are the empirical eigenvalues.

The low-order (coherent) representation consists of the $N = 6$ (CE) and $N = 7$ (OE) highly energetic modes. The coherent and residual contributions to the Reynolds stress tensor are defined as $\overline{u_{ci}u_{cj}}$ and $\overline{u_i''u_j''}$, respectively. By construction, their summation yields the total (RANS) Reynolds stress field:

$$\overline{u_i'u_j'} = \overline{u_{ci}u_{cj}} + \overline{u_i''u_j''}.$$

The N modes used were determined based on the contribution to $\overline{u_{ci}u_{cj}}$. Based on a cross-validation of the three independent trials, the contribution to the coherent stresses of other modes was below the experimental uncertainty and thus not statistically significant.

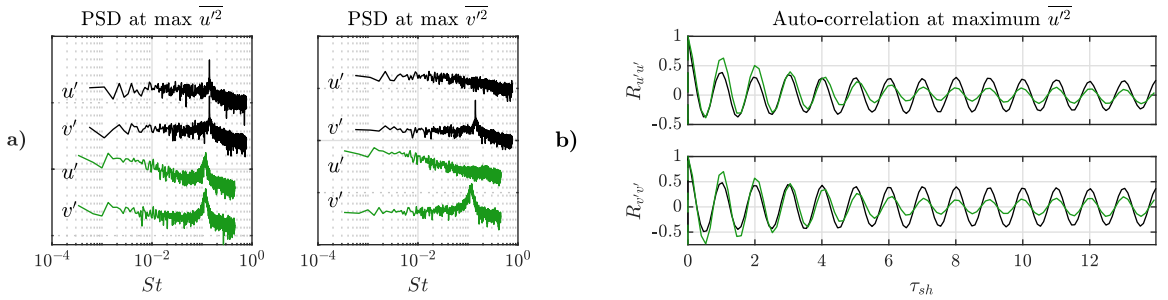

Figure 2. a) Power spectral density (PSD) function of u', v' at max $\overline{u'^2}$ (left), and $\overline{v'^2}$ (right). Spectra are off-set for clarity. b) Auto-correlations $R_{u'u'}$ (top), and $R_{v'v'}$ (bottom) at point of maximum $\overline{u'^2}$. OE (green); CE (black).

RESULTS

The quasi-periodic, turbulent near wake of a nominally two-dimensional (2D) thin flat plate normal to uniform oncoming stream is investigated for two conditions. Differences between the mean wakes arising due to the open and closed end conditions are briefly identified from the mean field. Subject to a POD modal analysis, slow-varying contributions to the wake dynamics are characterized. Finally, their influence on the turbulent wake structure is discussed.

Mean streamlines overlaying flooded contours of the principle Reynolds stresses ($\overline{u'^2}$, $\overline{v'^2}$, $\overline{u'v'}$) in the central plane, $z = 0$, are shown together with their coherent and residual field contributions in Fig. 1. Also shown are the $\overline{u'^2}, \overline{v'^2}$ and $\overline{w'^2}$ y-distributions at the locations of maximum $\overline{v'^2}$. It was verified that the mean flow field is 2D over at least $-10 < z/c < 10$ (W, $\overline{u'w'}$, $\overline{v'w'}$, and z-gradients of u, v, Reynolds stresses and mean base pressure vanish within experimental uncertainty). From preliminary flow visualizations, shedding is predominantly parallel in both cases.

The mean field shows mirror-symmetry about the plane $y = 0$. While the streamline topology is similar for both cases, the recirculation length measured along $y = 0$ to the saddle point at $x = \ell_R$, is significantly longer in the open end case, $\ell_R = 3.9c$, than for the closed end, $\ell_R = 2.4c$. Moreover, the curvature of the separation streamline, extending from the leading edges along the shear layer to the wake saddle point, is smaller for the open than the closed end case. Similar to the results of Narasimhamurthy & Andersson (2009), a reduction in ℓ_R and increase in curvature coincide with a lower base pressure and higher shedding frequency, suggesting changes in the dynamics.

The magnitude of the Reynolds stresses (RANS) are generally much larger with closed than with open ends. Downstream of the recirculation foci, the main contribution to the Reynolds stresses in both cases is from the coherent motion, ostensively related to the vortex shedding process. In this region, in contrast to the RANS field, the three residual field normal stresses are nearly equal, implying that the coherent field describes much of the wake anisotropy. Differences in the vortex formation process are suggested by the observations that: (i) the location of the maxima for $\overline{u'^2}$ and $\overline{v'^2}$ are located within the recirculation region for the closed end case, but outside for the open ends; (ii) in the base region upstream of the recirculation foci, the magnitude of the Reynolds stresses are generally high for the closed, but very low for the open end cases, respectively. In the base region, an inversion in the sign $\overline{u'v'}$ is only observed for the closed end case. The inversion is associated with the coherent contribution and is not observed in the residual field. For the open end case, the coherent contribution to the Reynolds shear stress is strongly dominant.

Spectra of the u' and v' velocity components at locations of maximum $\overline{u'^2}$ and $\overline{v'^2}$ are shown together with their auto-correlations in Fig. 2. In both cases, strong periodic contributions associated with vortex shedding occur at frequencies corresponding to $St = 0.119$ (OE) and $St = 0.141$ (CE). In contrast to the closed end case, the open case shows significant spectral broadening and a larger energy accumulation at low frequencies, which is consistent with a more rapid decay of the auto-correlation function. As discussed below, these results indicate a greater cycle-to-cycle variation in the wake for the open than the closed end case.

Figures 3 and 4 provide a succinct summary of key aspects of the POD analysis. The 6 (CE) or 7 (OE) contributing coherent energetic modes account for about 53% (CE) or 66% (OE) of the TKE (Fig. 3). The two most energetic modes, representing 46% (CE) and 54% (OE) of the TKE, show very strong spectral energy concentrations at the shedding frequency. Iso-contours of their u-spatial functions, $\mathbf{\Phi}^u_1, \mathbf{\Phi}^u_2$ – not shown for brevity, are anti-symmetric about $y = 0$ and show nearly-periodic spatial patterns in the x-direction. These are a fundamental harmonic pair, with temporal coefficients a_1 and a_2, as deduced by their phase relation in Fig. 4a. Within any arbitrary shedding cycle, the amplitude $A = \sqrt{a_1^2 + a_2^2}$ is nearly constant, but A varies between cycles. This amplitude modulation is significantly greater for the open end case. In the figure, the red line closely approximates A for the average shedding cycle. A mode pair, a_3 and a_4, corresponding to the second harmonic with spectral energy concentration at $2f_{sh}$, is observed in both fields (not shown for brevity). Their u spatial functions are symmetric about $y = 0$ and show streamwise spatial periodicity at about half the wave length observed for the fundamental pair. While the second harmonic pair contributes only about 3% of the TKE, its contribution to $\overline{u'^2}$ is significant, especially in regions about the symmetry plane.

The most energetic mode with a symmetric u-spatial modal function, $\mathbf{\Phi}^u_\Delta$, is associated with low-frequency spectral energy concentration, seen in spectra of a_Δ in Fig. 3. The amplitude of this slow-varying mode, a_Δ, is strongly coupled with the oscillation amplitude of the fundamental harmonic, a_1 and a_2. As seen from the a_Δ, a_2 phase portraits of Fig. 4b, the relationship takes the form of a paraboloid, $a_\Delta \approx c_0 + c_1 A^2$, with c_0 and c_1 constants. As a cautionary observation, it is noted that the parabolic regression line is not indicative of the trajectory in the phase space since, during a typical cycle, A varies little. This behaviour has been observed in other cylinder wake flows (Noack *et al.*, 2003; Bourgeois *et al.*, 2013) and has been interpreted as a conservative energy exchange between shed

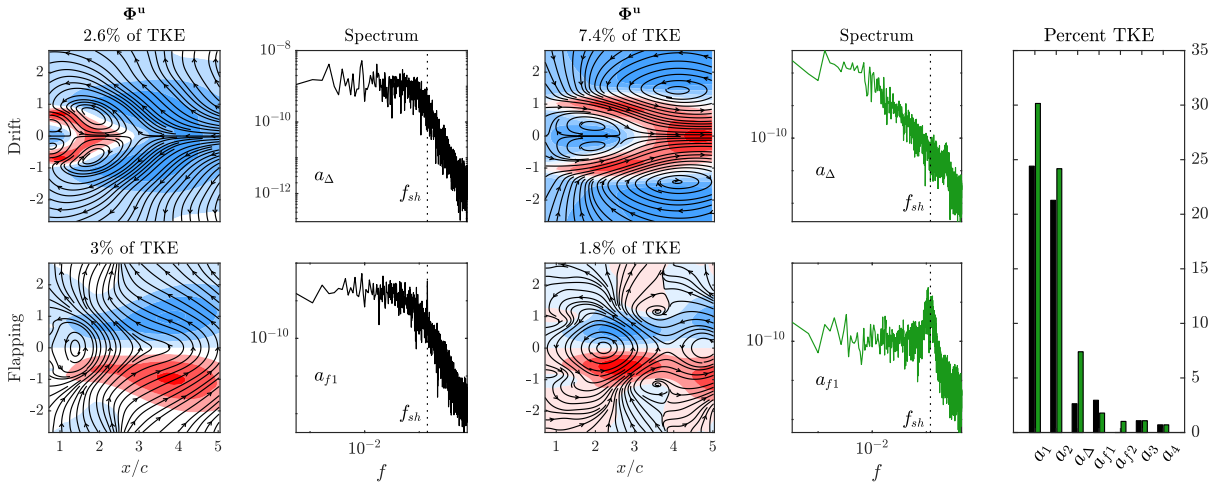

Figure 3. Flooded isocontours and pseudo-streamlines for spatial functions together with spectra of temporal coefficients for the slow drift, a_Δ (top), and flapping, a_{f1} (bottom), modes. CE is on the left, OE on the right. Spatial modes are orthonormal: $(\mathbf{\Phi}_n, \mathbf{\Phi}_m) = \delta_{nm}$. Right most: relative contribution to the TKE. a_1, a_2 fundemental harmonic pair. a_3, a_4 second harmonic.

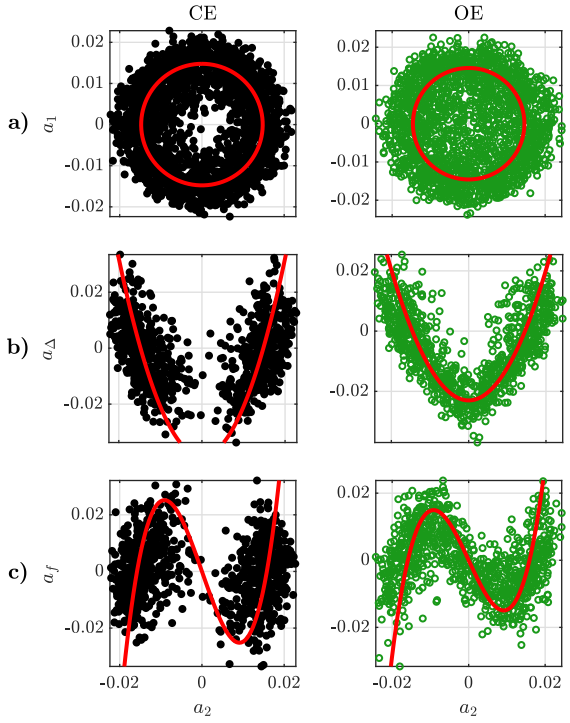

Figure 4. Phase portraits for CE (left) and OE (right) for: a) harmonic pair a_2 vs. a_1; b) a_2 vs. a_Δ, ($a_1 \approx 0$); and c) a_2 vs. a_f, ($a_1 \approx 0$). The red line indicates a regression in b) and c); in a) it indicates the limit cycle ($a_\Delta = 0$). The modal coefficients are scaled by $\sqrt{\lambda_n}$.

vortices and a slow-drift of the base flow. Here, the base flow is defined as: $\mathbf{u}_B = \mathbf{U} + \mathbf{u}_\Delta$, with $\mathbf{u}_\Delta = a_\Delta \mathbf{\Phi}_\Delta$.

Closer inspection of this modal relationship suggests differences in the wake dynamics. For the closed end case, the fluctuations are concentrated about the limit (mean) shedding cycle and represent only 2.6% of the TKE, suggesting low modulation of the shedding amplitude consistent with the narrow spectral peak of Fig. 2. For the open end case, a_Δ represents 7.4% of the TKE. The fluctuation extends from the limit cycle to the unstable equilibrium where $A \approx 0$, suggesting strong cycle-to-cycle modulation of the shedding process with intervals of vortex shedding suppression. These observations are consistent with the spectral broadening and loss of coherence seen in Fig. 2.

In both fields the third most energetic anti-symmetric mode is characterized by a u-spatial modal function which shows strong contributions along the separated shear layer (Fig. 3). These modes appear to be related to the dynamics of the shear layer.

For the closed end case, the spectrum of the temporal coefficients, a_{f1}, indicates energetic content at low frequencies together with a significant, but non-dominant contribution about f_{sh}. The peak at f_{sh} is sharp. This mode accounts for about 3% of the TKE, which is similar to that for a_Δ. For the open end case, significant spectral broadening is observed and the mode is relatively weaker, accounting for about 2% of the TKE, compared to 7.4% for a_Δ. It is noted that for the open end case, a weaker second mode, a_{f2} was identified, with similar characteristics to a_{f1} (albeit phase shifted in both time and space). The mode a_{f2} accounts for approximately 1% of the TKE, but its contribution to the coherent Reynolds stresses is not negligible. In subsequent discussion, a_{f1} and a_{f2} are considered as pairs.

A direct comparison of the open and closed end fields lends itself to ambiguous interpretation because these subtend dynamically different regions. Specifically, the PIV domain for the closed end case captures more of the wake dynamics since it extends to $2.12\ell_R$, whereas the open end field extends to $1.29\ell_R$, such that the recirculation region dynamics tend to be more heavily weighted. To maintain the same spatial resolution within the constraints of the experimental set-up, an additional PIV plane for the open end case was considered. This plane has the same dimensions and extends from $x = 0.87\ell_R$ to $2.13\ell_R$.

As observed from Fig. 5 for the extended field, the u-spatial modal function is very similar to that observed for the closed end case, while the spectrum that its temporal coefficients show is similar to those obtained upstream for the open end case, albeit the contribution at f_{sh} is weaker than observed upstream (Fig. 3). For the extended plane, a second flapping mode is not observed, suggesting that a_{f2} is more related to dynamics of the recirculation region. It is thus suggested that the third most energetic anti-symmetric

mode in the three fields relate to similar dynamics.

These modes show a strong coupling with the fundamental harmonic pair as deduced from the $a_{f1} - a_2$ phase relations in Fig. 4c and 5. A linear regression analysis suggests a relationship for both fields of the type $a_{f1} \approx (A^2 + c_2)(a_1 + a_2)$, with c_2 a constant. Tacitly implied is a link to a_Δ through $a_\Delta \approx c_0 + c_1 A^2$. Again, it is noted that the regression lines are not indicative of the trajectories in the phase space, as these are normal to the plane shown. About the limit cycle, where $a_\Delta \approx 0$, a_{f1} is strongly expressed. These observations suggest energetic exchanges between modes related to three distinct motions.

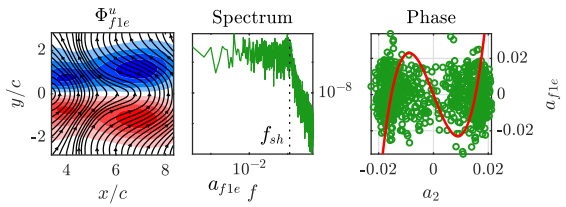

Figure 5. Left, u-spatial mode of the OE extended field flapping mode. Middle, spectrum of its temporal coefficients. Right, phase portrait of a_{f1e} vs. a_2 ($a_1 \approx 0$).

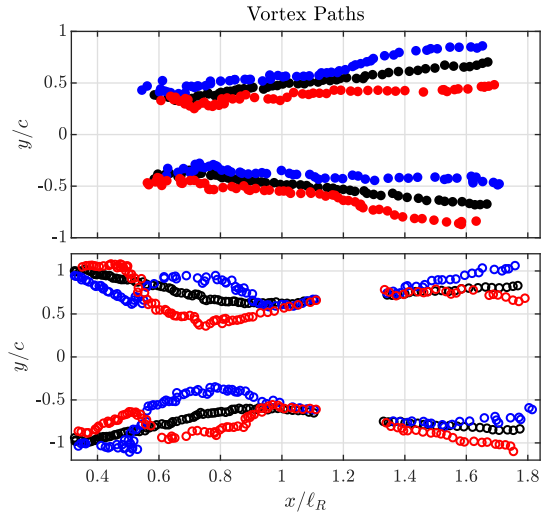

Figure 6. Phase averaged vortex trajectories for CE (top) and OE (bottom). Whitespace in OE paths separate near-field and extended-field. Black ▪ ▪ ▪ indicates the mean vortex paths. Blue ▪ ▪ ▪ and red ▪ ▪ ▪ indicate the positive and negative most flapping mode (a_f) contributions to the shedding cycle.

The mode shapes of $\mathbf{\Phi}^u_{f1}$ in Fig. 3 and in the extended field, $\mathbf{\Phi}^u_{f1e}$ in Fig. 5, appear to describe an in-tandem flow-normal oscillation, or a flapping motion, of the separated shear layers. The u-spatial modes are antisymmetric about $y = 0$. Hence, these modes tend to increase u in one shear layer, while decreasing u in the opposing one.

The influence of a flapping motion on the trajectories of shed vortices is illustrated in Fig. 6. The forming vortices are fed by circulation advected along the shear layers. Hence, their position is expected to follow the motion of the shear layers. Figure 6 shows the conditionally phase-averaged trajectory of the vortex cores, defined by the vorticity centroid, for different states of the flapping motion. Briefly, the shedding cycles were regrouped in three bins based on the magnitude of the modal coefficients expressing the flapping motion. In each of these bins, the phase space trajectories for each cycle are similar. The bins represent the positive most, median, and negative most flapping mode contributions to the shedding cycle. With each bin a phase average of the shedding cycle was then done. The influence of this flapping motion is most clearly visualized in the wake region downstream of the vortex formation region. For position extrema of a_{f1}, the vortex trajectories are biased upward ($y > 0$) and downwards ($y < 0$), while about the average ($a_f = 0$), they are symmetric about $y = 0$.

Within the recirculation region ($x/\ell_R < 1$), as can most clearly be seen in the open end case, the deflected vortex paths cross the average trajectories, and then reconverge near the end of the recirculation. It is noted for the closed end condition that within the recirculation region the three trajectories are also very close but the scatter lies within the uncertainty.

The low-frequency modes influence the vortex formation dynamics. For the open end case, the largest negative values of a_Δ coincide with the vertex of the paraboloid of Fig. 4b. During these intervals, the base flow recirculation and shear layers extend far downstream (Fig. 7a). The shear layer coupling is weakened, observed as $a_{f1} \approx 0$, indicating little flow-normal oscillation and resulting in a delayed formation of weaker vortices. Note that the plate base region is nearly stagnant. In contrast, close to the limit cycle, $a_\Delta \approx 0$, the base flow recirculation is shorter, the shear layer coupling stronger (contribution of a_{f1} increases) leading to a short formation length and stronger shed vortices (Fig. 7b). For the closed end case, the cycle-to-cycle variation a_Δ and a_{f1} are less significant, Fig. 4b, resulting in a shorter formation length and a more regular shedding of strong vortices (Fig. 7c). In considering the trajectories of Fig. 6 and the near wake formation, it appears that the energetic exchanges between the slow drift and flapping modes are more significant for the open than for the closed end case.

Figure 8a shows the distribution of $\overline{u'^2}$ and $\overline{v'^2}$ along $y = 0$. Note that x is normalized by ℓ_R to compare dynamically similar regions. As deduced from Fig. 8a, for the open end case vortices form considerably later in the recirculation region when compared to the closed end case. This observation is consistent with Fig. 1, showing that $\overline{u'^2}_{max}$ and $\overline{v'^2}_{max}$ occur downstream of the recirculation region for the open, but inside the recirculation for the closed ends. For the open end case, the flow is nearly stagnant immediately behind the plate. In contrast, for the closed end case, the vortices induce an impinging flow on the back face, resulting in much stronger Reynolds stresses. More dynamically important, whereas $\overline{u'^2}$ increases for the closed end case, it decreases for the open end case as the plate is approached.

The exact production term for a 2D-flow along $y = 0$, where $\overline{u'v'} = 0$, is given by $G_k = (\overline{v'^2} - \overline{u'^2})\frac{\partial U}{\partial x}$. In Fig 8b, the coherent and residual fields are compared. Generally, it is noted that the coherent contributions are largest and the peak production terms occur close to locations of maximum $\overline{v'^2}$ (Fig. 1). Note that in regions of low separation-streamline curvature (upstream of the recirculation foci in Fig. 1), production is negligible for the open end case. For the closed end case, coherent production is negative (energy is removed) which indicates a transfer of energy to the residual field consistent with the Reynolds stress distribution ob-

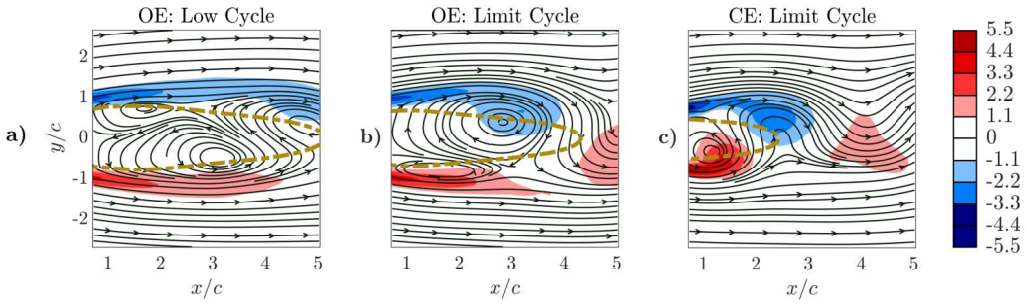

Figure 7. Low-order (coherent) representation of vorticity iso-contours overlaid with instantaneous streamlines at a similar shedding phase: a) open end (OE) for minimum a_Δ (low cycle) and b) limit cycle; c) closed end (CE) limit cycle. The gold lines indicate $\boldsymbol{u}_B = \boldsymbol{U} + \boldsymbol{u}_\Delta = 0$.

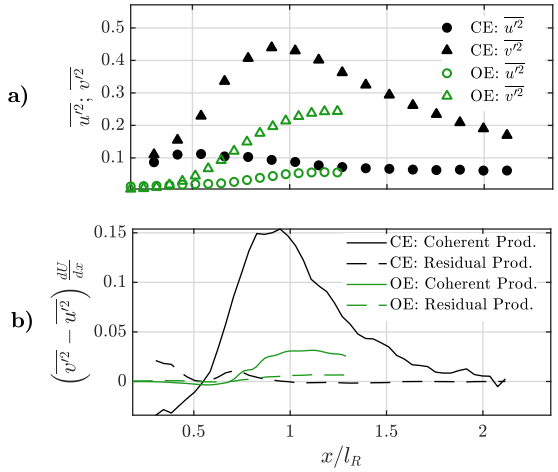

Figure 8. a) RANS field Reynolds stress and b) coherent and residual production along $y = 0$ for open (OE) and closed (CE) ends as functions of x/ℓ_R.

served in Fig. 1. These results appear consistent with the energy exchanges discussed in relation to Fig. 6. For the open end case, conservative fluctuation energy exchanges occur between slow drift and flapping modes, while for the closed ends, interactions with the back face of the plate enhance transfer to the residual field.

CONCLUDING REMARKS

A comparative study of the turbulent, quasi-periodic wake of a 2D thin flat plate normal to a uniform stream for open and closed end conditions was presented. Following a POD analysis, the wake structure of the spatial modes for these flows was found to be similar. The temporal coefficients suggest a strong coupling between modes representing a slow-varying base flow, a_Δ, shear layer flapping, a_{f1}, and a mode-pair corresponding to the fundamental shedding frequency. Considered in the phase space, the form of these relationships are similar between the two cases.

However, the level of contribution of respective modes differ significantly between wakes. These results suggest that while similar mechanisms occur in both wakes, their relative strength differs, resulting in significant changes in the observed wake dynamics, mean velocity and Reynolds stress fields. A plausible explanation is that the open ends allow for the ambient pressure to be imposed on the recirculation region, leading to a higher base pressure (lower drag). In turn the curvature of the separated streamline is reduced thus weakening energy transfer to the flapping mode.

REFERENCES

Bourgeois, J. A., Noack, B. R. & Martinuzzi, R. J. 2013 Generalized phase average with applications to sensor-based flow estimation of the wall-mounted square cylinder wake. *Journal of Fluid Mechanics* **736**, 316–350.

Fage, A. & Johansen, F. C. 1927 On the flow of air behind an inclined flat plate of infinite span. In *Proceedings of the Royal Society of London. Series A* (ed. H. Lamb), , vol. 116, pp. 170–197. Royal Society.

Hammache, M. & Gharib, M. 1991 An experimental study of the parallel and oblique vortex shedding from circular cylinders. *Journal of Fluid Mechanics* **232**, 567–590.

Hemmati, A., Wood, D. H. & Martinuzzi, R. J. 2016 Effect of side-edge vortices and secondary induced flow on the wake of normal thin flat plates. *International Journal of Heat and Fluid Flow* **61**, 197–212.

Hemmati, A., Wood, D. H. & Martinuzzi, R. J. 2018 On simulating the flow past a normal thin flat plate. *Journal of Wind Engineering and Industrial Aerodynamics* **174**, 170–187.

Kiya, M. & Matsumura, M. 1988 Incoherent turbulence structure in the near wake of a normal plate. *Journal of Fluid Mechanics* **190**, 343–356.

Lisoski, D. L. A. 1993 Nominally 2-dimensional flow about a normal flat plate. PhD thesis, California Institute of Technology, Pasadena, CA.

Mohebi, M., Wood, D. H. & Martinuzzi, R. J. 2017 The turbulence structure of the wake of a thin flat plate at post-stall angles of attack. *Experiments in Fluids* **58**, 67.

Najjar, F. M. & Balachandar, S. 1998 Low-frequency unsteadiness in the wake of a normal flat plate. *Journal of Fluid Mechanics* **370**, 101–147.

Narasimhamurthy, V. D. & Andersson, H. I. 2009 Numerical simulation of the turbulent wake behind a normal flat plate. *International Journal of Heat and Fluid Flow* **30**, 1037–1043.

Noack, B. R., Afanasiev, K., Morzyński, M., Tadmor, G. & Thiele, F. 2003 A hierarchy of low-dimensional models for the transient and post-transient cylinder wake. *Journal of Fluid Mechanics* **497**, 335–363.

Williamson, C. H. K. 1989 Oblique and parallel modes of vortex shedding in the wake of a circular cylinder at low reynolds numbers. *Journal of Fluid Mechanics* **206**, 579–627.